

Review

High-Performance Ligand-Protected Metal Nanocluster Catalysts for CO₂ Conversion through the Exposure of Undercoordinated Sites

Dominic Alfonso 

National Energy Technology Laboratory, U.S. Department of Energy, Pittsburgh, PA 15236, USA; alfonso@netl.doe.gov

Abstract: Previous experimental breakthroughs reveal the potential to create novel heterogeneous catalysts for the electroreduction of CO₂ to a high-value product CO using ligand-protected Au-based nanoclusters. Since the chemical composition and geometric structures have been precisely defined, it is possible to adopt robust design guidelines for the development of practical catalysts and to fundamentally elucidate the underlying reaction mechanism. In this short review, the computational progress made to understand the experimentally observed reduction process on the following subset of materials—Au₂₅(SR)₁₈[−], Au₂₄Pd(SR)₁₈, Au₂₃(SR)₁₆[−] and Au₂₁Cd₂(SR)₁₆[−]—is described. A significant finding from our first-principles mechanistic studies is that CO₂ conversion on the fully ligand protected nanoclusters is thermodynamically unfavorable due to the very weak binding of intermediates on the surface region. However, the reaction becomes feasible when either Au or S sites are exposed through the removal of a ligand. The results particularly point to the role of undercoordinated S sites in the creation of highly functional heterogeneous catalysts that are both active and selective for the CO₂ conversion process. The incorporation of dopants could significantly influence the catalytic reactivity of the nanoclusters. As demonstrated in the case of the monopalladium substitution in Au₂₅(SR)₁₈[−], the presence of the foreign atom leads to an enhancement of CO production selectivity due to the greater stabilization of the intermediates. With the Cd substitution doping of Au₂₃(SR)₁₆[−], the improvement in performance is also attributed to the enhanced binding strength of the intermediates on the geometrically modified surface of the nanocluster.

Keywords: computational electrocatalysis; CO₂ conversion; nanostructured functional materials; structural disorder



Citation: Alfonso, D. High-Performance Ligand-Protected Metal Nanocluster Catalysts for CO₂ Conversion through the Exposure of Undercoordinated Sites. *Catalysts* **2022**, *12*, 505. <https://doi.org/10.3390/catal12050505>

Academic Editor: C. Heath Turner

Received: 7 March 2022

Accepted: 28 April 2022

Published: 30 April 2022

Publisher's Note: MDPI stays neutral with regard to jurisdictional claims in published maps and institutional affiliations.



Copyright: © 2022 by the author. Licensee MDPI, Basel, Switzerland. This article is an open access article distributed under the terms and conditions of the Creative Commons Attribution (CC BY) license (<https://creativecommons.org/licenses/by/4.0/>).

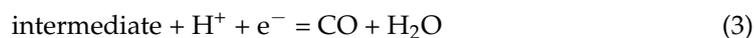
1. Introduction

The relentless warming trend caused by human greenhouse CO₂ emission, primarily from burning fossil fuels, is regarded as an alarming measure of the Earth's altered climate. The consequence is visible in the local and regional extreme weather events that are disruptive to modern life. Despite a global agreement to strengthen climate commitments, the overall CO₂ emission is on track to keep rising, unless a range of effective technologies is developed and deployed. The electro-reduction of captured greenhouse gas CO₂ is a promising class of electrochemical transformation in the broad scheme of carbon capture and utilization [1–12]. Powered by renewable electricity, it can potentially mitigate the increasing level of CO₂ in the atmosphere, while providing a promising pathway towards sustainable and clean CO₂ upgrade into a high value product at mild conditions. Among the economically viable products from this process is CO due to its intrinsic properties and its role as a starting reagent in other synthetic pathways.

The electrochemical reduction of CO₂ (CO₂RR) to CO involves two major steps occurring at the interface between the cathode and electrolyte:



Each step involves the transfer of an electron, as the reactant is transformed into a product:



The first proton–electron transfer step involves the activation of C–O bonds to form the related intermediate. In the second step, the intermediate rearranges to products followed by desorption from the surface of the catalyst into the electrolyte. The proton–electron pair originates from the water splitting in the anode:



The above process could be sustainable if driven electrochemically using electrical energy from renewable sources, such as wind and solar [13–15].

CO₂RR, however, presents major performance challenges in terms of efficiency as a particular intractable issue is the CO₂ molecule being fully oxidized and thermodynamically stable. Although the equilibrium redox potential of CO₂ to CO is merely −0.11 V vs. the reversible hydrogen electrode (RHE), a larger overpotential (defined as the difference between the equilibrium potential and the onset or practical potential) of about −1 V is required due to the significant cost of disrupting the CO₂ bonds [2]. When a far larger overpotential is applied, the undesirable hydrogen evolution reaction (HER) competes with CO₂RR in the aqueous system generating H₂ as a side product. Thus, the acceleration of the kinetics of CO₂RR and the concomitant suppression of the competing HER are of great significance for large scale applications.

Facilitating efficiency and selectivity can be promoted via the rational design of effective electrocatalysts. Transition metal nanoparticles (NPs) of transition metals are explored for CO₂RR as these materials have a quite solid track record of being used as catalysts for other related reactions, such as CO oxidation [16,17], the oxygen reduction reaction [18–21] and purely HER [22,23]. Among transition metals, the noble metal Au and Ag stand out in exclusively reducing CO₂ to CO. Their excellent mechanical property permits the fabrication of materials with a different size, shape and component to improve CO₂RR performance. A cyclic voltammetry experiment on a 200 nm Ag NP revealed a current density peak at a moderate overpotential of about −0.75 V associated with CO production [24]. The feature grows as the NP shrinks from 200 to 1 nm, indicating that the rate of CO₂ conversion is sensitive to the particle size. Varying the shape also plays a role as evidenced by an experimentally reported Ag nanoporous catalyst that is very selective for CO products [25]. The current density shows a 300-fold increase over its polycrystalline counterpart at an overpotential of ≤−0.5 V. Based on the powder X-ray diffraction pattern, the observed enhancement is linked to an increase in the number of under-coordinated facets. This is attributed to the favorable binding of the intermediates, resulting in smaller overpotentials needed to overcome the thermodynamic barrier. Experiments on triangular Ag nanoplates with predominant Ag(100) yield a 96.8% selectivity under −0.86 V [26]. Size effect is also utilized to tune the catalytic activity and selectivity of Au NPs [27]. Differently sized NPs ranging from 4 to 10 nm show a prominent size-dependent activity/selectivity in the CO₂RR with the 8 nm NP reaching a Faradaic efficiency (FE) of 90% at −0.67 V. Based on density functional theory (DFT) calculations, CO evolution is more favored on the edge sites, while the competitive HER is more active on the corner sites. A significant conclusion is the activity/selectivity of Au NPs can be tuned by varying the size to optimize the ratio of corner and edge sites. A similar conclusion was reached for the size-dependent catalytic activity studies of Au NPs in the size range of ~1–8 nm [28]. A dramatic increase in current density, albeit with a decrease in selectivity for CO, was observed, with decreasing Au particle size. The DFT calculations revealed that changes in the population of low-coordinated edge sites with a stronger chemisorption property are responsible for the upsurge in HER activity.

An emerging strategy is to explore the use of a new class of nanomaterials, the ligand-protected Au-based nanoclusters (NCs). Unlike conventional NPs, these materials

exhibit well-defined atomic structures with 10–100 metal atoms in the underlying inorganic core that form selective bonds with ligand stabilizers [29–32]. As in a few atom clusters, these exhibit molecular-like electronic structures owing to strong quantum confinements effects [33,34]. They are reported to promote the thermal oxidation of styrene-, CO- and sulfur-containing compounds [35–38]. Thiolate-protected NCs consisting of 25 gold atoms in the core region ($\text{Au}_{25}(\text{SR})_{18}^-$, where SR is the thiolate ligand) are the first NCs to be tested for CO_2RR [39]. Under aqueous conditions, CO FE reaches nearly 100% at -1.0 V, which is a marked improvement over conventional Au NPs and bulk Au electrodes. It was found that the charged state and the electrochemical catalytic activity are strongly correlated, with the negatively charged species showing the best CO_2RR activity, followed by its neutral and the positively charged counterparts [40,41]. The monopalladium-doped NC $\text{Au}_{24}\text{Pd}(\text{SR})_{18}$ was reported to achieve nearly 100% CO FE at potential ranging from -0.6 V to -1.2 V, a marked improvement over the pristine species whose FE declines beginning at -0.9 V. $\text{Au}_{19}\text{Cd}_2(\text{SR})_{16}^-$, a doped counterpart of $\text{Au}_{23}(\text{SR})_{16}^-$, made by introducing Cd atoms in the exterior portion, was reported to further promote CO_2RR with CO selectivity of 90–95% at -0.5 to -0.9 V. This material exhibits the highest CO_2RR activity (2200 mA mg^{-1} at -1.0 V) among the reported NCs.

Obtaining a full understanding of the reaction mechanisms responsible for CO_2RR on these NCs is of great interest from a fundamental standpoint, providing complementary data points for the rational design of materials. Since it is not yet plausible to observe the reaction pathways experimentally, it is necessary to explore theoretical avenues. The precise atomic structures available from crystallographic data have made it possible to gain important mechanistic insights into the CO_2 conversion on these NCs using theoretical simulation. It also permits further investigation into the synergistic effects on the reaction mechanism brought about by alloying. In the next section, we review our previous complementary theoretical simulation, showing how the outcome helps to shape a mechanistic understanding of CO_2RR on these materials.

2. Theoretical Studies of Au-Based Nanoclusters

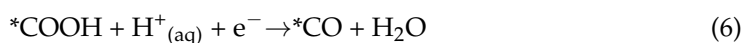
2.1. Aspects of Modeling

A particular aspect of the modelling of CO_2RR is the quantification of binding strength between a given catalyst and the intermediates. The binding states of the adsorbates are influenced not only by the constituent elements of the catalyst, but also the nature of the active sites and any chemical additives. Hence, calculation is an effective strategy that could potentially unveil structure-activity relationships. In what follows, we provide a description of the modeling approaches used for CO_2RR to CO on pertinent Au-based NCs under an electrochemical environment.

The thermodynamics for electrochemical reactions were obtained using the computational hydrogen electrode (CHE) approach [42]. At the heart of this technique is the assumption that the free energy of the proton–electron pair ($G_{\text{H}^+ + \text{e}^-}$) is equal to that of the hydrogen gas ($\frac{1}{2} G_{\text{H}_2(\text{g})}$) at potential $U = 0$ V at 101,325 Pa of H_2 , 298 K and all pH values. When $U \neq 0$ V, a potential linear shift of $-eU$ is applied on the free energy. For a proton–electron transfer to adsorbate *A , $^*A + \text{H}^+_{(\text{aq})} + \text{e}^- \rightarrow ^*AH$, the free energy change becomes $\Delta G(U) = G_{^*AH} - G_{^*A} - \frac{1}{2} G_{\text{H}_2(\text{g})} + eU$, where $G_{^*AH}$, $G_{^*A}$, $G_{\text{H}_2(\text{g})}$ and e are the free energy of the product, free energy of the reactant, free energy of gas phase H_2 and the elementary positive charge, respectively. For a given reaction step, the limiting potential U_L is obtained, which is defined as the value that makes it exothermic, $\Delta G \leq 0$ eV. For a reaction pathway, the corresponding limiting potential is given by the step with the highest reaction free energy. A key assumption is that the proton–electron transfer barrier in each step is assumed to be surmountable at room temperature as the appropriate potential is applied.

The pathway towards CO production may take the following 2e^- CO_2RR mechanism [43,44]:





In these formulae, the adsorption of CO_2 is accompanied by coupling with an electron/proton pair to initiate the catalysis reaction. The $*\text{CO}$ intermediate stems from $*\text{COOH}$ after electron/proton transfer and the removal of water. In the last step, the adsorbed CO formed in the second reduction step undergoes molecular desorption. For the competing HER reaction, the 2e^- pathway producing H_2 may be represented by [28,45]:



In this mechanism, a hydronium ion initially adsorbs on the surface and forms a hydrogen radical, followed by combination of two hydrogen radicals to form a hydrogen molecule. The limiting potentials for H_2 evolution $U_L(\text{H}_2)$ and CO_2 reduction $U_L(\text{CO}_2)$ were determined numerically according to $-\left\{\frac{\max(\Delta G(8), \Delta G(9))}{e}\right\}$ and $-\left\{\frac{\max(\Delta G(5), \Delta G(6))}{e}\right\}$, respectively. In order not to be severely contaminated by HER, the limiting potential of this process should be as negative as possible compared to CO_2RR . The descriptor that represents the difference in the limiting potentials, $U_L(\text{CO}_2) - U_L(\text{H}_2)$, can then be used to ascertain the trend in selectivity. That is, a positive value corresponds to preference for CO_2RR and the more positive the magnitude becomes, the higher its selectivity over HER.

The relaxation of the geometry was performed using the DFT approach. The employed DFT method was implemented using the Vienna Ab Initio Simulation Package (VASP) [46]. The exchange-correlation functional used in this study was based in the framework of Perdew, Burke and Ernzerhof [47], while the core-electrons were represented by the projector-augmented wave (PAW) method [48]. The Kohn-Sham one electron valence eigenstates were expanded in terms of plane-wave basis sets with a cutoff energy of 500–600 eV. The ionic and electronic convergence limit were set to 0.03 eV/Å and 1×10^{-5} eV, respectively, while the Methfessel-Paxton scheme [49] was utilized with a smearing width of 0.1 eV. A three-dimensional periodic cubic box with 30 Å side was inserted in the simulation models to minimize unphysical interactions. The sampling of the Brillouin zone was conducted with a Γ -point k -point mesh.

The Poisson-Boltzmann implicit solvent model implemented in VASP by Matthew and Hennig was employed [50]. The background dielectric constant of water was set to $\epsilon_b \sim 80$ with a cutoff charge density of 0.0025 \AA^{-3} . The cavitation energies were evaluated employing a surface tension parameter of 0.525 meV/\AA^2 . Free energy corrections for adsorbed species were applied assuming harmonic degrees of freedom and those for gaseous species were quantified in the ideal gas limit. The free energy for the aqueous species was evaluated by applying free energy corrections to their room temperature state.

2.2. Theoretical Insights

2.2.1. Carbon Dioxide Reduction on $\text{Au}_{25}(\text{SR})_{18}^-$

In this section, our group's effort to understand the mechanistic pathways of CO_2RR to CO on $\text{Au}_{25}(\text{SR})_{18}^-$ is presented. The experimental work of Kauffman et al. brought $\text{Au}_{25}(\text{SR})_{18}^-$ to the spotlight where it was demonstrated that the NC is active in CO_2RR . It can successfully reduce CO_2 to CO beginning with an overpotential of -0.19 V (Figure 1A) [39,40], indicating that $\text{Au}_{25}(\text{SR})_{18}^-$ is superior to Au nanoparticles and bulk Au by 0.2–0.3 V. The FE for selective CO production reaches approximately 100% at -1.0 V (Figure 1B), which shows that almost every electron injected is harnessed in the conversion process. Additionally, the CO formation rate is 7–700 times higher than the conventional Au NPs and bulk Au electrodes at this industrially relevant potential. The corresponding neutral and positively charged counterparts, $\text{Au}_{25}(\text{SR})_{18}$ and $\text{Au}_{25}(\text{SR})_{18}^+$, yield comparable products and onset potentials. However, the current density, turnover frequency and FE are higher in $\text{Au}_{25}(\text{SR})_{18}^-$.

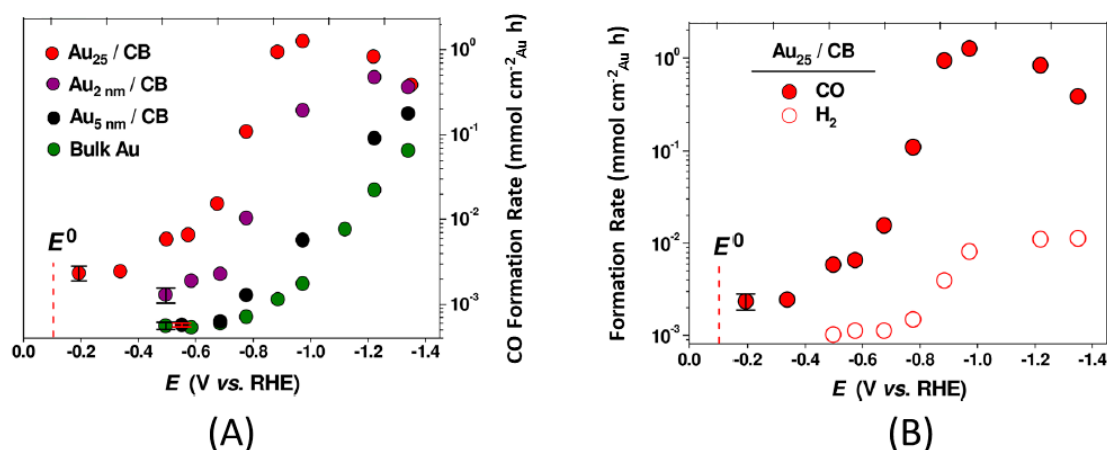


Figure 1. (A) Potential-dependent FE for CO on $\text{Au}_{25}(\text{SR})_{18}^-$ nanoclusters, Au nanoparticles of 2 and 5 nm size, and bulk gold electrode. (B) Potential dependent FE for CO and H_2 formation on $\text{Au}_{25}(\text{SR})_{18}^-$ nanoclusters. Adapted from Reference [39]. Copyright 2012 by the American Chemical Society.

Though the experimental structures of the NCs are available experimentally, simulation models that perfectly match the data can become computationally prohibitive. For example, $\text{Au}_{25}(\text{SR})_{18}^-$ would require a 349-atom representation when each of the 18-atom ligand ($-\text{SR} = -\text{SCH}_2\text{CH}_2\text{C}_6\text{H}_5$) is included. Moreover, for plane-wave basis sets with a typical energy cutoff of 500–600 eV, a sizeable periodic box to blot out any unphysical effect due to image interaction needs to be employed.

To remedy this, we utilized a methyl thiolate ($-\text{SCH}_3$) to represent the real ligand, thereby reducing the model to a relatively manageable 115 atom representation [39]. The use of a truncated version of the ligands can be traced back to a previous DFT work in which a smaller $-\text{SH}$ ligand representation is used [51]. Our model is an upgrade in that it mimics better the overall electronegativity of $-\text{SCH}_2\text{CH}_2\text{C}_6\text{H}_5$. With a viable and realistic atomic representation at hand, we explored the active sites in the intact nanocluster. With CO_2 as the adsorbate, our calculations identified several configurations with binding energies of up to -0.2 eV. The most energetically favorable structure consisted of the oxygen end of CO_2 interacting with three adjacent sulfur atoms (Figure 2). However, the theoretical picture of a weak CO_2 binding was problematic since the adsorbed molecule could desorb at ambient temperature. At this juncture, we were guided by the prevailing conjecture that the active sites were located on the intact NC [35–38].

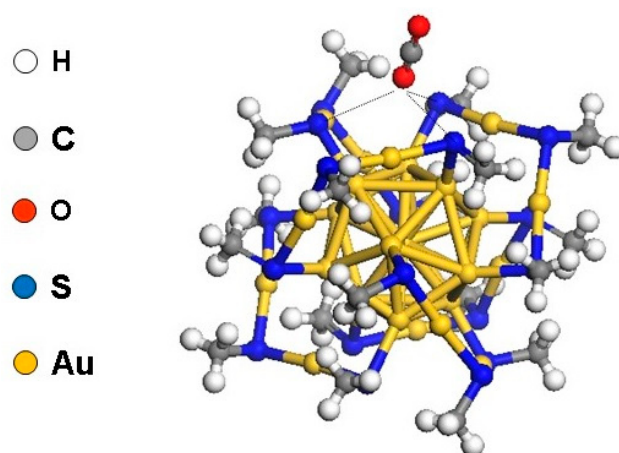


Figure 2. CO_2 adsorbed on $\text{Au}_{25}(\text{SCH}_3)_{18}^-$ nanocluster. Adapted from Reference [39]. Copyright 2012 by the American Chemical Society.

With our initial foray providing a practical $\text{Au}_{25}(\text{SCH}_3)_{18}^-$ model, baseline data and further intuition, we then embarked on more comprehensive studies to refine our understanding. Merely looking at the initial CO_2 adsorption offers a very limited picture of the process. Other aspects, such as the subsequent chemical transformation, including the reaction thermodynamics, need to be addressed. In the follow up studies, we looked at the reaction profile using the widely used CHE method [52]. We also took into account previous efforts showing both the inactivity of the intact nanocluster in the context of thermal CO oxidation [35], and the critical role of undercoordinated sites as the driving force for aldehyde hydrogenation and other oxidation reactions [53,54].

The free energy profile for the reaction pathway based on CO_2RR steps outlined in Section 2.1 and the optimized intermediate structures on the intact NC are displayed in Figure 3. For an external potential of $U = 0$ V, the protonation of CO_2 to form COOH is endothermic, requiring 2.04 eV, while the dissociation of the protonated COOH is exothermic. After surface CO is formed, it can detach with a small barrier to form the gas phase molecule. The COOH formation is the potential limiting step with an overpotential of -2.04 V. However, this is about one order of magnitude larger than the experimental value at which the initiation of CO production is observed (~ -0.1 V) [39]. A significant finding is that CO_2RR is unlikely to occur in intact form at room temperature and low overpotentials.

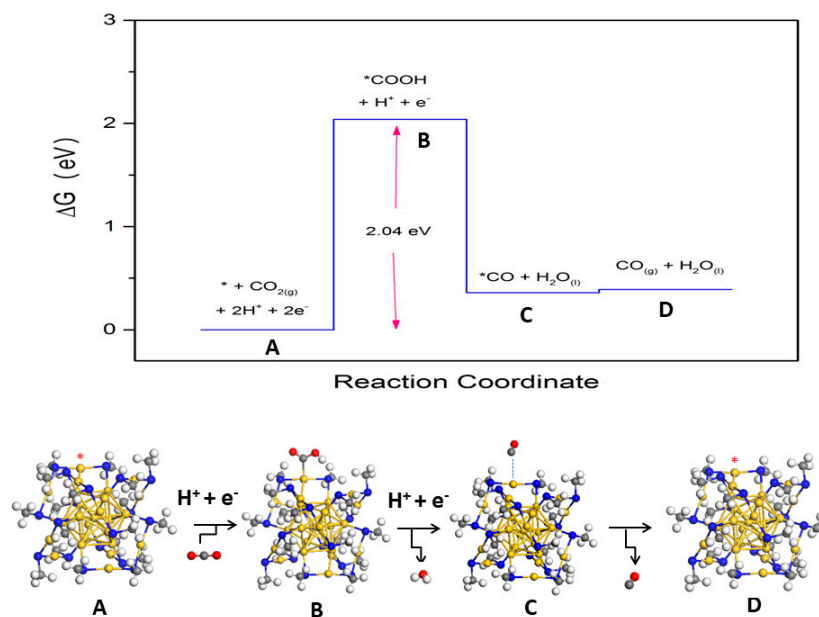


Figure 3. Free energy profile of the CO_2 reduction to CO in the intact $\text{Au}_{25}(\text{SCH}_3)_{18}^-$ nanocluster. Adapted from Reference [52]. Copyright by The American Institute of Physics (2016).

The suggestion that undercoordinated atoms in the negatively charged nanocluster promoted thermal aldehyde hydrogenation and other oxidation reactions opened new vistas for further exploration [35,53,54]. For example, in situ IR and complementary DFT calculations showed the intact NC as inert for thermal CO oxidation [35]. Oxidation took place when a defect was introduced on the surface region through the partial removal of ligands. This was a vivid indicator of property-structure relationships in that the improved performance was attributed to the presence of a defect termination with low coordination numbers.

The CO_2RR process was reexamined by generating via a single dethiolation yielding undercoordinated Au as the active site. The energies required for the formation of the adsorbed intermediates ($^*\text{COOH}$ and $^*\text{CO}$) were predicted to be dramatically lower than the intact case (Figure 4). The lower limit of the overpotential associated with the first reduction step was predicted to be -0.34 V, which was in better agreement with the measured value. The possibility of a non-metal S site as the reaction center provides an alternative scenario [55]. Instead of the whole ligand, only the hydrocarbon portion

was removed, producing a defect consisting of an exposed S atom. Undercoordinated S atoms were also proposed as active sites for cubane-shaped Ni–Fe–S [56], and MoS₂ catalysts [57]. An endothermic and exothermic ΔG for the electrochemical formation of Au and S sites, respectively, were predicted indicating that the stripping away of CH₃ is more thermodynamically favorable. A significant finding is that the S site for CO₂ reduction was also active for H₂ evolution. To gain further insight into the selectivity trend, Austin et al. used the descriptor $U_L(\text{CO}_2) - U_L(\text{H}_2)$, where the first and second term refer to limiting potentials for CO₂RR and HER. Unlike the Au site, CO₂RR was predicted to be selective on the S site as evidenced by the positive $U_L(\text{CO}_2) - U_L(\text{H}_2)$ value [55]. Thus, an improved coupling between theory and experiments was attained when the S site was considered as the reaction center.

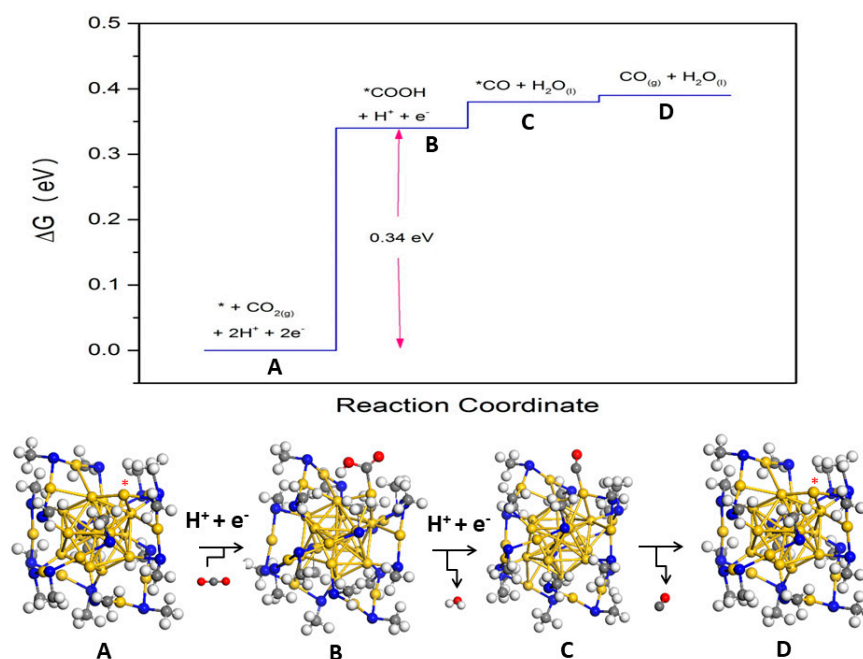


Figure 4. Free energy profile of the CO₂ reduction to CO on the dethiolated Au₂₅(SCH₃)₁₈[−] nanocluster Adapted from Reference [52]. Copyright by the American Institute of Physics (2016).

2.2.2. Promotion of Carbon Dioxide Reduction through Doping

We explored the incorporation of dopant as an approach to facilitate CO₂RR. From the scanning tunneling electron microscopy (STEM) images, both size and significant morphology can be ruled out upon monopalladium substitution in Au₂₅(SR)₁₈[−], namely, the monodispersed ~0.8 nm size was essentially preserved (Figure 5A,B). In situ spectroscopy analysis combined with CHE calculations revealed that the substitution promoted electroreduction activity and selectivity [58]. Figure 6A–C show the measured electrochemical CO₂RR activity of Au₂₄Pd(SR)₁₈ versus Au₂₅(SR)₁₈, indicating CO and H₂ as the primary products of both materials. The potential-dependent CO FE showed a significant amount of the molecule was generated, reaching approximately 100% at a potential range of −0.6 to −0.9 V. Beyond −0.9 V, the catalytic performance of Au₂₅(SR)₁₈ decreased, whereas the doped counterpart was not significantly compromised. The CO partial current density also revealed that Au₂₄Pd(SR)₁₈ exhibited higher CO partial current density and mass activity at the same conditions. Unlike conventional Au NPs and bulk Au electrodes, Au₂₄Pd(SR)₁₈ is capable of attaining 100% CO FE over a much wider potential range and a near-complete HER suppression up to −1.2 V. Moreover, it possesses a high stability even under the negative potential for CO₂RR (Figure 6D). Thus, doping the parent NC with a Pd atom can elevate both activity and selectivity.

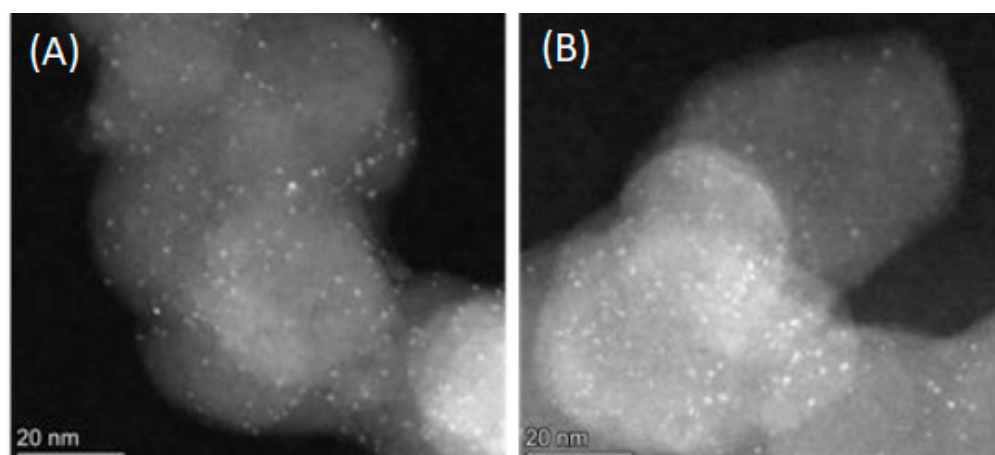


Figure 5. STEM images of (A) Au₂₅ and (B) Pd₁Au₂₄. Adapted from Ref. [58]. Copyright by the American Chemical Society (2020).

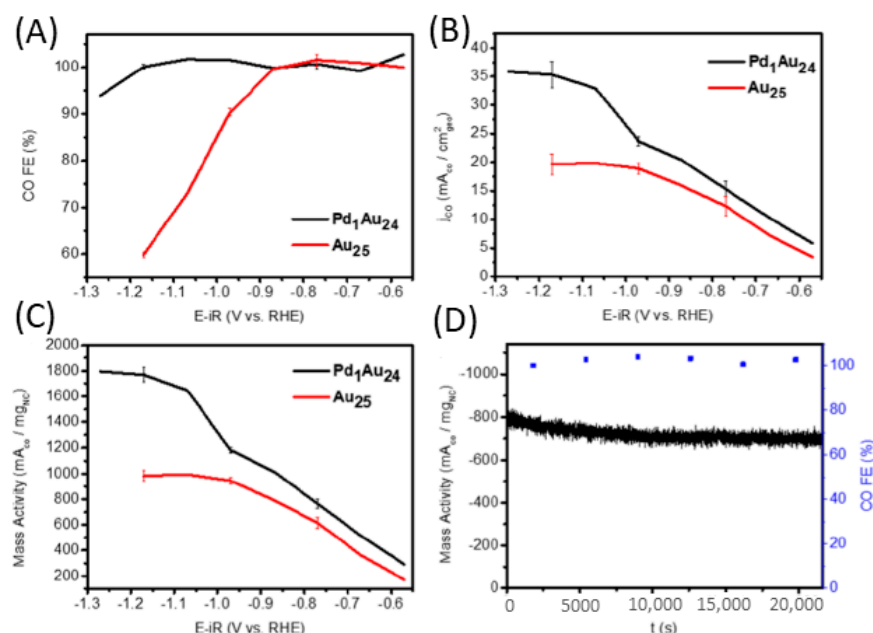


Figure 6. (A) FE for CO production. (B) CO partial current density. (C) CO mass activity. (D) Stability test of Pd₁Au₂₄ at -0.8 V for 6 h. Au₂₅ and Pd₁Au₂₄ represent Au₂₅(SR)₁₈ and Au₂₄Pd(SR)₁₈, respectively. Adapted from Reference [58]. Copyright by the American Chemical Society (2020).

A significant conclusion drawn in Section 2.2.1 is that the intact cluster can be ruled out as an active catalyst, highlighting the role of undercoordinated sites in facilitating CO₂RR. The removal of one of the thiol ligands unveils a reactive metal site that lowers the formation of the crucial COOH intermediate for CO₂ reduction. Another feasible scenario is also predicted, namely, the electrochemical displacement of the hydrocarbon portion of the thiol ligand to form an exposed S as the reaction center. We used Au₂₅(SCH₃)₁₈ and Au₂₄Pd(SCH₃)₁₈ simulation models to represent the intact parent and the doped NCs and removed the SCH₃ and CH₃ portions to expose Au and S sites. The calculations predicted that the Pd atom prefers to reside in the core site of the activated NCs, and the spatial preference did not change in the presence of the CO, COOH and H intermediates.

Figure 7A,B summarize the predicted free energy diagram of CO₂RR and HER on the exposed metal site of Au₂₅(SCH₃)₁₇ and Au₂₄Pd(SCH₃)₁₇. In both cases, the potential limiting step for CO₂RR was predicted to be the first electron/proton transfer step. The binding of the COOH intermediate in the doped NC was slightly stronger than the parent

NC, resulting in the lowering of the potential requirement ($U_L(\text{CO}_2) = -0.58$ V compared to $U_L(\text{CO}_2) = -0.67$ for the parent NC). For HER, the protonation of adsorbed H to form gaseous H_2 is predicted to be the step that dictates the potential requirements since it occurs at positive free energy. The limiting potential in the pure case ($U_L(\text{H}_2) = -0.08$ V) is lower than the doped one ($U_L(\text{H}_2) = -0.17$ V). The predicted $U_L(\text{CO}_2) - U_L(\text{H}_2)$ for the parent and the doped version are -0.59 V and -0.41 V, suggesting that selective CO_2 reduction is not favorable on the exposed metal site.

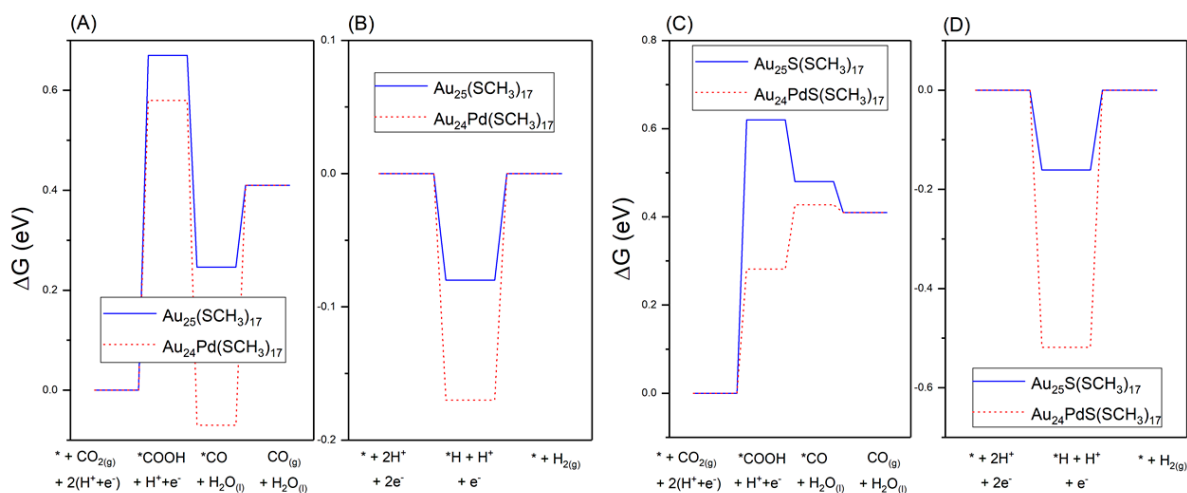


Figure 7. Free energy diagram of for electrochemical reduction of (A) CO_2 RR and (B) HER on the bare metal site of the dethiolated $\text{Au}_{25}(\text{SCH}_3)_{18}$ and $\text{Au}_{24}\text{Pd}(\text{SCH}_3)_{18}$ nanoclusters. The free energies of (C) CO_2 RR and (D) HER on the sulfur site of the demethylated nanoclusters are included for comparison.

Since the above calculations ruled out the possibility of selective CO_2 reduction on the metal site, the alternate scenario involving exposed sulfur as the active site was considered. The calculated CO_2 RR and HER free energy diagrams in Figure 7C,D show the first electrochemical step as the limiting step of CO_2 RR in both NCs. While the formation of $^* \text{COOH}$ species still required an increase in free energy, the key difference was the enhanced stability of this intermediate on sulfur. The adsorption of both COOH and H intermediates were found to be more favorable than on the Au site. On both NCs, the electrochemical H_2 desorption remained to be the potential limiting step since it was the most endothermic step. The calculated $U_L(\text{CO}_2) - U_L(\text{H}_2)$ yielded values of -0.45 and 0.24 V for $\text{Au}_{25}\text{S}(\text{SCH}_3)_{17}$ and $\text{Au}_{24}\text{PdS}(\text{SCH}_3)_{17}$. Although our results showed that the $\text{Au}_{25}\text{S}(\text{SCH}_3)_{17}$ cluster can be active for CO_2 RR, it is only the $\text{Au}_{24}\text{PdS}(\text{SCH}_3)_{17}$ that is selective to CO_2 RR due to the positive value of $U_L(\text{CO}_2) - U_L(\text{H}_2)$. Thus, we find that the Pd dopant can play a critical role in stabilizing the key intermediates that better facilitates CO_2 RR. Moreover, the presence of the dopant leads to a more selective CO production when the reaction center consists of exposed S sites.

Another approach explored was to exclusively dope the NC surface without compromising the inner kernel metal structure of the parent material. Our work on the surface level modification of $\text{Au}_{23}(\text{SR})_{16}$ through doubly Cd substitution revealed that this was a viable scheme [59]. The CO_2 RR activities of the $\text{Au}_{23}(\text{SR})_{16}^-$ and $\text{Au}_{19}\text{Cd}_2(\text{SR})_{16}^-$ NCs were compared by conducting constant-potential electrolysis measurements at various applied potentials. It was found that the surface-doped version exhibited higher current densities for CO production (Figure 8B) and turnover frequencies with reduced onset potential (Figure 8C) than the undoped case. The doped version yielded CO as the major product between -0.5 and -0.9 V with HER becoming more competitive for potentials larger than -0.9 V (Figure 8A,D). In contrast, H_2 production was more dominant in the undoped version at all potentials. Notably, $\text{Au}_{19}\text{Cd}_2(\text{SR})_{16}^-$ demonstrates a larger CO partial current density than the previously reported Au NC and Au NP [59]. The ~ 40 mA/cm^2 value at -0.9 V is superior to the $2\text{--}18$ mA/cm^2 values reported for $\text{Au}_{44}(\text{TBBT})_{28}$, $\text{Au}_{47}\text{Cd}_2$

(TBBT)₃₁ (TBBT = tert-butylbenzenethiolate) and ultrathin Au–Pd nanocrystals at the same potential [60,61]. Additionally, the partial current density of ~45 mA/cm² at –1.0 V is about 33–90% higher than Au NP, Mo-doped Au NP and Au NP containing a CeO_x interface [62–64].

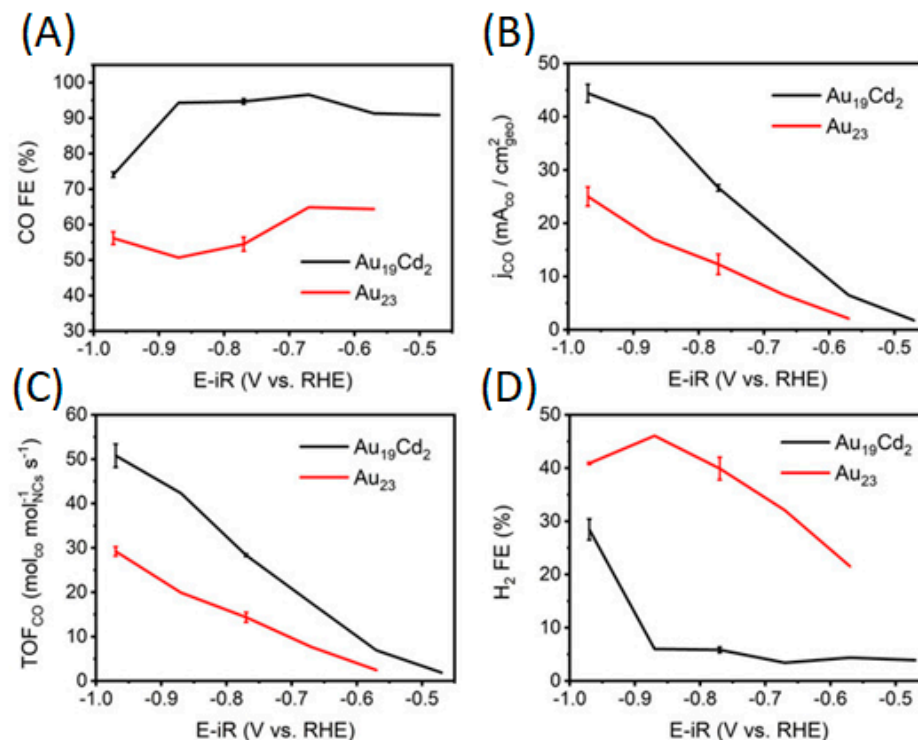


Figure 8. (A) FE for CO production. (B) CO partial current density. (C) TOF of CO₂RR. (D) FE for H₂ production. The error bar represents the mean and variance for 3 runs to check the reproducibility. Au₂₃ and Au₁₉Cd₂ represent Au₂₃(SR)₁₆[−] and Au₁₉Cd₂(SR)₁₆[−], respectively. Adapted from Reference [59]. Copyright by Wiley-VCH (2021).

Figure 9A,B show the structure of the model Au₂₃S(SCH₃)₁₅[−] and Au₁₉Cd₂S(SCH₃)₁₅[−] NCs containing exposed S as the active site, generated through the removal of a –CH₃ from Au₂₃(SCH₃)₁₆[−] and Au₁₉Cd₂(SCH₃)₁₆[−]. The predicted CO₂RR and HER energy profiles are depicted in Figure 9C,D. It is noted that the HER energy profiles for both NCs are comparable. While the CO₂RR step was predicted to be the potential limiting for both NCs, the process is less thermodynamically challenging in the doped case due to the stronger binding of CO. The calculated $U_L(\text{CO}_2) - U_L(\text{H}_2)$ for the doped version was predicted to be more positive by ~0.9 V, in agreement with the experimental selectivity trend.

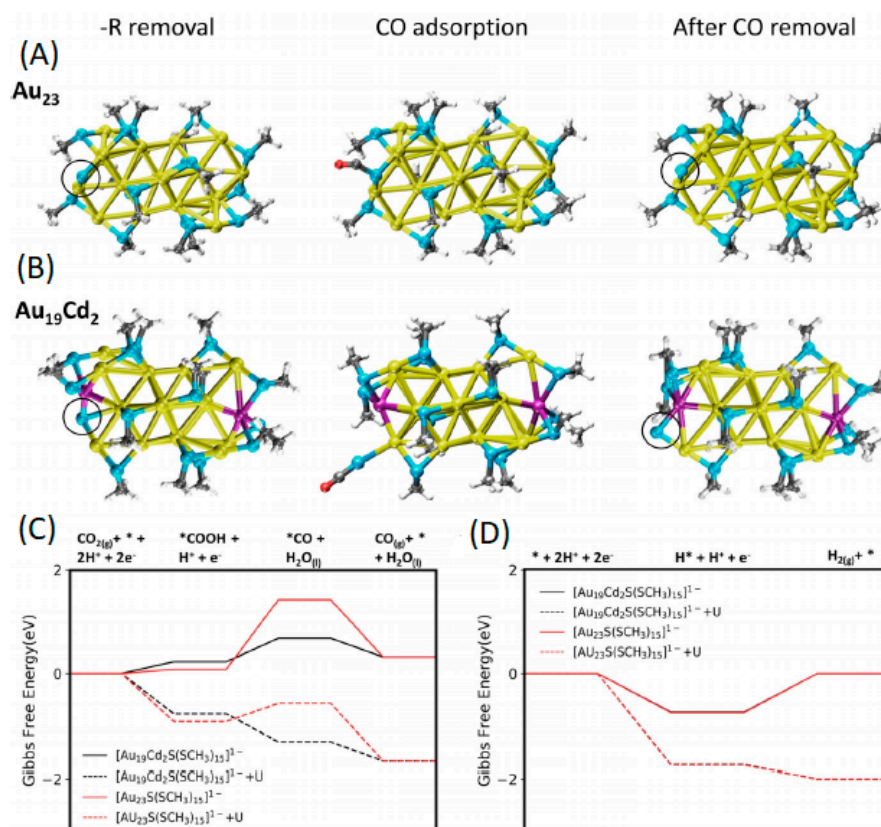


Figure 9. Optimized structures of (A) Au₂₃(SR)₁₆⁻ and (B) Au₁₉Cd₂(SR)₁₆⁻, upon -R(CH₃) removal, CO adsorption and CO removal. Atom colors: Au: yellow, Cd: pink, S: blue, C: black, H: white. Black circle demonstrates S active site. Reaction pathway for (C) CO₂RR and (D) HER on the Au₂₃(SR)₁₆⁻ (red lines) and Au₁₉Cd₂(SR)₁₆⁻ (black lines) upon -CH₃ removal. Solid lines represent free energy without an applied potential, while dotted lines represent those with an applied potential of -1.0 V vs. RHE. Adapted from Reference [59]. Copyright by Wiley-VCH (2021).

3. Summary and Outlook

In this short review, we described the complementary theoretical efforts to understand the experimentally observed CO₂RR activity and selectivity in Au₂₅(SR)₁₈⁻, Au₂₄Pd(SR)₁₈, Au₂₃(SR)₁₆⁻ and Au₂₁Cd₂(SR)₁₆⁻. We focused on a particular structural variation—ligand removal—and how it alters the CO₂RR activity and selectivity on the nanoclusters. The first-principles studies indicated that exposed S sites, possibly created during preparation or under reaction conditions, may be the active reaction center in all the NCs investigated. In contrast to the Au site, it stabilizes the pertinent CO₂RR intermediates while destabilizing H, yielding a non-negative $U_L(\text{CO}_2) - U_L(\text{H}_2)$. These results provide insights into the structure–property relationship in that the thermodynamics of the electrochemistry can be correlated to the undercoordinated S surface sites as the reaction center.

Further work must still be performed to elevate our fundamental understanding of the CO₂RR mechanism on these NCs. We note that much of our focus is on the determination of reaction energetics and thermodynamics. The availability of algorithms to simulate the hydrogenation by H⁺ + e⁻ species presents an opportunity to evaluate the reaction barriers under reaction conditions [65,66]. The obtained kinetic picture will lead to an increased coupling with experimental data, such as the measured current densities, which otherwise cannot be achieved by merely looking at the thermodynamics. Such effort may be challenging because of the huge computational expenses required to predict the reaction barriers within the DFT framework. The widely used Climbing Image Nudged Elastic Band (CI-NEB) method, for example, entails the discretization of the reaction pathway into a finite number of images to locate the transition state [67]. For the NCs considered

in this paper, the calculation using plane wave basis sets can become more expensive as each image would contain the NC model enclosed in a periodic box large, enough to cancel out spurious interaction. Additionally, explicit water molecules may have to be included in the images to account for the $H^+ + e^-$ transfer to the target intermediates, potentially requiring many hundreds of energies and gradients evaluations. However, continuing advances in high performance computing technology may expand the scope of first-principles simulations towards such type of explorations.

From a practical standpoint, more research remains to be pursued for Au-based NCs to realize its full potential. At present, the electrocatalysts considered in this review have not been integrated to practical devices to further evaluate their potential for the low-cost and scalable deployment for CO_2 conversion to CO. Such setup would permit the evaluation of the integrity of the materials at realistic conditions. Aside from the Au NCs, membrane materials and electrocatalyst's support are integral to the device. To comprehend the potential role of these components in determining the outcome of the CO_2 conversion, it is necessary to invest effort into this aspect. The introduction of non-aqueous electrolytes plus the optimization of other conditions, such as flow rate and pressure, may significantly enhance the performance metrics as well. Thus, while there is always a need for fundamental research, a future focus that would pave the way for a practical CO_2 conversion to CO application is highly desirable.

Funding: This researcher received no external funding.

Acknowledgments: This project was funded by the United States Department of Energy, National Energy Technology Laboratory. This report was prepared as an account of work sponsored by an agency of the United States Government. Neither the United States Government nor any agency thereof, nor any of their employees, makes any warranty, express or implied, or assumes any legal liability or responsibility for the accuracy, completeness, or usefulness of any information, apparatus, product, or process disclosed, or represents that its use would not infringe privately owned rights. Reference herein to any specific commercial product, process, or service by trade name, trademark, manufacturer, or otherwise does not necessarily constitute or imply its endorsement, recommendation, or favoring by the United States Government or any agency thereof. The views and opinions of author(s) expressed herein do not necessarily state or reflect those of the United States Government or any agency thereof.

Conflicts of Interest: The authors declare no conflict of interest.

References

1. Sakakura, T.; Choi, J.-C.; Yasuda, H. Transformation of carbon dioxide. *Chem. Rev.* **2007**, *107*, 2365. [[CrossRef](#)] [[PubMed](#)]
2. Hori, Y. Electrochemical CO_2 Reduction on Metal Electrodes. In *Modern Aspects of Electrochemistry*; Vayenas, C.G., White, R.E., Gamboa-Aldeco, M.E., Eds.; Springer: New York, NY, USA, 2008.
3. Mikkelsen, M.; Jørgensen, M.; Krebs, F.C. The teraton challenge. A review of fixation and transformation of carbon dioxide. *Energy Environ. Sci.* **2010**, *3*, 43–81. [[CrossRef](#)]
4. Wang, W.; Wang, S.; Ma, X.; Gong, J. Recent advances in catalytic hydrogenation of carbon dioxide. *Chem. Soc. Rev.* **2011**, *40*, 3703. [[CrossRef](#)] [[PubMed](#)]
5. Qiao, J.; Liu, Y.; Hong, F.; Zhang, J. A review of catalysts for the electroreduction of carbon dioxide to produce low-carbon fuels. *Chem. Soc. Rev.* **2014**, *43*, 631–675. [[CrossRef](#)] [[PubMed](#)]
6. Benson, E.E.; Kubiak, C.P.; Sathrum, A.J.; Smieja, J.M. Electrocatalytic and homogeneous approaches to conversion of CO_2 to liquid fuels. *Chem. Soc. Rev.* **2009**, *38*, 89–99. [[CrossRef](#)]
7. Zhang, W.; Hu, Y.; Ma, L.; Zhu, G.; Wang, Y.; Xue, X.; Chen, R.; Yang, S.; Jin, Z. Progress and perspective of electrocatalytic CO_2 reduction for renewable carbonaceous fuels and chemicals. *Adv. Sci.* **2018**, *5*, 1700275. [[CrossRef](#)]
8. Dry, M.E. The fischer—Tropsch process: 1950–2000. *Catal. Today* **2002**, *71*, 227–241. [[CrossRef](#)]
9. Schulz, H. Short history and present trends of Fischer—Tropsch synthesis. *Appl. Catal. A* **1999**, *186*, 3–12. [[CrossRef](#)]
10. Lan, G.; Yang, J.; Ye, R.P.; Boyjoo, Y.; Liang, J.; Liu, X.; Li, Y.; Liu, J.; Qian, K. Sustainable carbon materials toward emerging applications. *Small Methods* **2021**, *5*, 2001250. [[CrossRef](#)]
11. Liu, J.; Cai, C.; Wang, Y.; Liu, Y.; Huang, L.; Tian, T.; Yao, Y.; Wei, J.; Chen, R.; Zhang, K. A biomimetic plasmonic nanoreactor for reliable metabolite detection. *Adv. Sci.* **2020**, *7*, 1903730. [[CrossRef](#)]
12. Zu, Y.; Yao, H.; Wang, Y.; Yan, L.; Gu, Z.; Chen, C.; Gao, L.; Yin, W. The age of bioinspired molybdenum-involved nanozymes: Synthesis, catalytic mechanisms, and biomedical applications. *View* **2021**, *2*, 20200188. [[CrossRef](#)]

13. Chu, S.; Majumdar, A. Opportunities and challenges for a sustainable energy future. *Nature* **2012**, *488*, 294–303. [[CrossRef](#)] [[PubMed](#)]
14. Graves, C.; Ebbesen, S.D.; Mogensen, M.; Lackner, K.S. Sustainable hydrocarbon fuels by recycling CO₂ and H₂O with renewable or nuclear energy. *Renew. Sustain. Energy Rev.* **2011**, *15*, 1–23. [[CrossRef](#)]
15. Singh, M.R.; Clark, E.L.; Bell, A.T. Thermodynamic and achievable efficiencies for solar-driven electrochemical reduction of carbon dioxide to transportation fuels. *Proc. Natl. Acad. Sci. USA* **2015**, *112*, E6111–E6118. [[CrossRef](#)]
16. Lopez, N.; Nørskov, J.K. Catalytic CO oxidation by a gold nanoparticle: A density functional study. *J. Am. Chem. Soc.* **2002**, *124*, 11262–11263. [[CrossRef](#)]
17. Lopez, N.; Janssens, T.; Clausen, B.; Xu, Y.; Mavrikakis, M.; Bligaard, T.; Nørskov, J.K. On the origin of the catalytic activity of gold nanoparticles for low-temperature CO oxidation. *J. Catal.* **2004**, *223*, 232–235. [[CrossRef](#)]
18. Liang, Y.; Li, Y.; Wang, H.; Zhou, J.; Wang, J.; Regier, T.; Dai, H. Co₃O₄ nanocrystals on graphene as a synergistic catalyst for oxygen reduction reaction. *Nat. Mater.* **2011**, *10*, 780–786. [[CrossRef](#)]
19. Yang, H.; Vogel, W.; Lamy, C.; Alonso-Vante, N. Structure and electrocatalytic activity of carbon-supported Pt–Ni alloy nanoparticles toward the oxygen reduction reaction. *J. Phys. Chem. B* **2004**, *108*, 11024–11034. [[CrossRef](#)]
20. Chen, S.; Ferreira, P.J.; Sheng, W.; Yabuuchi, N.; Allard, L.F.; Shao-Horn, Y. Enhanced activity for oxygen reduction reaction on “Pt₃Co” nanoparticles: Direct evidence of percolated and sandwich-segregation structures. *J. Am. Chem. Soc.* **2008**, *130*, 13818–13819. [[CrossRef](#)]
21. Mazumder, V.; Chi, M.; More, K.L.; Sun, S. Core/shell Pd/FePt nanoparticles as an active and durable catalyst for the oxygen reduction reaction. *J. Am. Chem. Soc.* **2010**, *132*, 7848–7849. [[CrossRef](#)]
22. Li, Y.; Wang, H.; Xie, L.; Liang, Y.; Hong, G.; Dai, H. MoS₂ nanoparticles grown on graphene: An advanced catalyst for the hydrogen evolution reaction. *J. Am. Chem. Soc.* **2011**, *133*, 7296–7299. [[CrossRef](#)] [[PubMed](#)]
23. Popczun, E.J.; McKone, J.R.; Read, C.G.; Biacchi, A.J.; Wiltrout, A.M.; Lewis, N.S.; Schaak, R.E. Nanostructured nickel phosphide as an electrocatalyst for the hydrogen evolution reaction. *J. Am. Chem. Soc.* **2013**, *135*, 9267–9270. [[CrossRef](#)] [[PubMed](#)]
24. Salehi-Khojin, A.; Jhong, H.-R.M.; Rosen, B.A.; Zhu, W.; Ma, S.; Kenis, P.J.; Masel, R.I. Nanoparticle silver catalysts that show enhanced activity for carbon dioxide electrolysis. *J. Phys. Chem. C* **2013**, *117*, 1627–1632. [[CrossRef](#)]
25. Lu, Q.; Rosen, J.; Zhou, Y.; Hutchings, G.S.; Kimmel, Y.C.; Chen, J.G.; Jiao, F. A selective and efficient electrocatalyst for carbon dioxide reduction. *Nat. Commun.* **2014**, *5*, 3242. [[CrossRef](#)] [[PubMed](#)]
26. Liu, S.; Tao, H.; Zeng, L.; Liu, Q.; Xu, Z.; Liu, Q.; Luo, J.-L. Shape-dependent electrocatalytic reduction of CO₂ to CO on triangular silver nanoplates. *J. Am. Chem. Soc.* **2017**, *139*, 2160–2163. [[CrossRef](#)] [[PubMed](#)]
27. Zhu, W.; Michalski, R.; Metin, O.; Lv, H.; Guo, S.; Wright, C.J.; Sun, X.; Peterson, A.A.; Sun, S. Monodisperse Au Nanoparticles for Selective Electrocatalytic Reduction of CO₂ to CO. *J. Am. Chem. Soc.* **2013**, *135*, 16833–16836. [[CrossRef](#)] [[PubMed](#)]
28. Mistry, H.; Reske, R.; Zeng, Z.; Zhao, Z.-J.; Greeley, J.; Strasser, P.; Roldan Cuenya, B. Exceptional Size—Dependent Activity Enhancement in the Electroreduction of CO₂ over Au Nanoparticles. *J. Am. Chem. Soc.* **2014**, *136*, 16473–16476. [[CrossRef](#)]
29. Gates, B.C. Supported gold catalysts: New properties offered by nanometer and sub-nanometer structures. *Chem. Commun.* **2013**, *49*, 7876–7877. [[CrossRef](#)]
30. Herzing, A.A.; Kiely, C.J.; Carley, A.F.; Landon, P.; Hutchings, G.J. Identification of active gold nanoclusters on iron oxide supports for CO oxidation. *Science* **2008**, *321*, 1331–1335. [[CrossRef](#)]
31. Corma, A.; Concepción, P.; Boronat, M.; Sabater, M.J.; Navas, J.; Yacaman, M.J.; Larios, E.; Posadas, A.; López-Quintela, M.A.; Buceta, D. Exceptional oxidation activity with size-controlled supported gold clusters of low atomicity. *Nat. Chem.* **2013**, *5*, 775–781. [[CrossRef](#)]
32. Oliver-Meseguer, J.; Cabrero-Antonino, J.R.; Domínguez, I.; Leyva-Pérez, A.; Corma, A. Small gold clusters formed in solution give reaction turnover numbers of 107 at room temperature. *Science* **2012**, *338*, 1452–1455. [[CrossRef](#)] [[PubMed](#)]
33. Alvarez, M.M.; Khoury, J.T.; Schaaff, T.G.; Shafiqullin, M.N.; Vezmar, I.; Whetten, R.L. Optical absorption spectra of nanocrystal gold molecules. *J. Phys. Chem. B* **1997**, *101*, 3706–3712. [[CrossRef](#)]
34. Jin, R. Quantum sized, thiolate-protected gold nanoclusters. *Nanoscale* **2010**, *2*, 343–362. [[PubMed](#)]
35. Wu, Z.; Jiang, D.-E.; Mann, A.K.; Mullins, D.R.; Qiao, Z.-A.; Allard, L.F.; Zeng, C.; Jin, R.; Overbury, S.H. Thiolate ligands as a double-edged sword for CO oxidation on CeO₂ supported Au₂₅ (SCH₂CH₂Ph)₁₈ nanoclusters. *J. Am. Chem. Soc.* **2014**, *136*, 6111–6122. [[CrossRef](#)]
36. Gaur, S.; Wu, H.; Stanley, G.G.; More, K.; Kumar, C.S.; Spivey, J.J. CO oxidation studies over cluster-derived Au/TiO₂ and AUROLite™ Au/TiO₂ catalysts using DRIFTS. *Catal. Today* **2013**, *208*, 72–81. [[CrossRef](#)]
37. Zhu, Y.; Qian, H.; Zhu, M.; Jin, R. Thiolate-Protected Au_n Nanoclusters as Catalysts for Selective Oxidation and Hydrogenation Processes. *Adv. Mater.* **2010**, *22*, 1915–1920. [[CrossRef](#)]
38. Nie, X.; Qian, H.; Ge, Q.; Xu, H.; Jin, R. CO oxidation catalyzed by oxide-supported Au₂₅(SR)₁₈ nanoclusters and identification of perimeter sites as active centers. *ACS Nano* **2012**, *6*, 6014–6022. [[CrossRef](#)]
39. Kauffman, D.; Alfonso, D.; Matranga, C.; Qian, H.; Jin, R. Experimental and Computational Investigation of Au₂₅ Clusters and CO₂: A Unique Interaction and Enhanced Electrocatalytic Activity. *J. Am. Chem. Soc.* **2012**, *134*, 10237–10243. [[CrossRef](#)]
40. Kauffman, D.R.; Alfonso, D.; Matranga, C.; Ohodnicki, P.; Deng, X.; Siva, R.C.; Zeng, C.; Jin, R. Probing active site chemistry with differently charged Au₂₅^q nanoclusters (q = −1, 0, +1). *Chem. Sci.* **2014**, *5*, 3151–3157. [[CrossRef](#)]

41. Vickers, J.W.; Alfonso, D.; Kauffman, D.R. Electrochemical carbon dioxide reduction at nanostructured gold, copper, and alloy materials. *Energy Technol.* **2017**, *5*, 775–795. [[CrossRef](#)]
42. Norskov, J.K.; Rossmeisl, J.; Logadottir, A.; Linqvist, L.; Kitchin, J.R.; Bligaard, T.; Jonsson, H.J. Origin of the overpotential for oxygen reduction at a fuel-cell cathode. *Phys. Chem. B* **2004**, *108*, 17886–17892. [[CrossRef](#)]
43. Peterson, A.A.; Abild-Pedersen, F.; Studt, F.; Rossmeisl, J.; Norskov, J.K. How Copper Catalyzes the Electroreduction of Carbon Dioxide into Hydrocarbon Fuels. *Energy Environ. Sci.* **2010**, *3*, 1311–1315. [[CrossRef](#)]
44. Hansen, H.A.; Varley, J.B.; Peterson, A.A.; Nørskov, J.K. Understanding trends in the electrocatalytic activity of metals and enzymes for CO₂ reduction to CO. *J. Phys. Chem. Lett.* **2013**, *4*, 388–392. [[CrossRef](#)]
45. Zhu, W.; Zhang, Y.-J.; Zhang, H.; Lv, H.; Li, Q.; Michalsky, R.; Peterson, A.A.; Sun, S. Active and selective conversion of CO₂ to CO on ultrathin Au nanowires. *J. Am. Chem. Soc.* **2014**, *136*, 16132–16135. [[CrossRef](#)] [[PubMed](#)]
46. Kresse, G.; Furthmüller, J. Efficiency of Ab-Initio Total Energy Calculations for Metals and Semiconductors Using a Plane-Wave Basis Set. *Comp. Mat. Sci.* **1996**, *6*, 15–50.
47. Perdew, J.P.; Burke, K.; Enzerhof, M. Generalized Gradient Approximation Made Simple. *Phys. Rev. Lett.* **1996**, *77*, 3865–3868. [[CrossRef](#)]
48. Kresse, G.; Joubert, D. From Ultrasoft Pseudopotentials to the Projector Augmented Wave Method. *Phys. Rev. B* **1999**, *59*, 1758–1775. [[CrossRef](#)]
49. Methfessel, M.; Paxton, A.T. High Precision Sampling for Brillouin Zone Integration for Metals. *Phys. Rev. B* **1989**, *40*, 3616–3621. [[CrossRef](#)]
50. Matthew, K.; Sundararaman, R.; Lechtworth-Weaver, K.; Arias, T.A.; Hennig, R.J. Implicit solvation model for density-functional study of nanocrystal surfaces and reaction pathways. *Chem. Phys.* **2014**, *140*, 84106. [[CrossRef](#)]
51. Lopez-Acevedo, O.; Kacprzak, K.A.; Akola, J.; Hakkinen, H. Quantum size effects in ambient CO oxidation catalysed by ligand-protected gold clusters. *Nat. Chem.* **2010**, *2*, 329–334. [[CrossRef](#)]
52. Alfonso, D.; Kauffman, D.; Matranga, C.J. Active sites of ligand-protected Au₂₅ nanoparticle catalysts for CO₂ electroreduction to CO. *Chem. Phys.* **2016**, *144*, 184705. [[CrossRef](#)] [[PubMed](#)]
53. Li, G.; Abroshan, H.; Chen, Y.; Jin, R.; Kim, H.J. Experimental and mechanistic understanding of aldehyde hydrogenation using Au₂₅ nanoclusters with Lewis acids: Unique sites for catalytic reactions. *J. Am. Chem. Soc.* **2015**, *137*, 14295–14304. [[CrossRef](#)] [[PubMed](#)]
54. Zhang, B.; Kaziz, S.; Li, H.; Hevia, M.G.; Wodka, D.; Mazet, C.; Burgi, T.; Barrabés, N. Modulation of Active Sites in Supported Au₃₈(SC₂H₄Ph)₂₄ Cluster Catalysts: Effect of Atmosphere and Support Material. *J. Phys. Chem. C* **2015**, *119*, 11193–11199. [[CrossRef](#)]
55. Austin, N.; Zhao, S.; McKone, J.; Jin, R.; Mpourmpakis, G. Elucidating the active sites for CO₂ electroreduction on ligand-protected Au₂₅ nanoclusters. *Catal. Sci. Technol.* **2018**, *8*, 3795–3805. [[CrossRef](#)]
56. Varley, J.; Hansen, H.; Ammitzbøll, N.L.; Grabow, L.; Peterson, A.; Rossmeisl, J.; Nørskov, J. Ni-Fe-S cubanes in CO₂ reduction electrocatalysis: A DFT study. *ACS Catal.* **2013**, *3*, 2640–2643. [[CrossRef](#)]
57. Chan, K.; Tsai, C.; Hansen, H.A.; Norskov, J. Molybdenum Sulfides and Selenides as Possible Electrocatalysts for CO₂ Reduction. *ChemCatChem* **2014**, *6*, 1899. [[CrossRef](#)]
58. Li, S.; Alfonso, D.; Nagarajan, A.V.; House, S.D.; Yang, J.C.; Kauffman, D.R.; Mpourmpakis, G.; Jin, R. Monopalladium substitution in gold nanoclusters enhances CO₂ electroreduction activity and selectivity. *ACS Catal.* **2020**, *10*, 12011–12016. [[CrossRef](#)]
59. Li, S.; Nagarajan, A.V.; Alfonso, D.R.; Sun, M.; Kauffman, D.R.; Mpourmpakis, G.; Jin, R. Boosting CO₂ electrochemical reduction with atomically precise surface modification on gold nanoclusters. *Angew. Chem. Int. Ed.* **2021**, *60*, 6351–6356. [[CrossRef](#)]
60. Zhuang, S.; Chen, D.; Liao, L.; Zhao, Y.; Xia, N.; Zhang, W.; Wang, C.; Yang, J.; Wu, Z. Hard-sphere random close-packed Au₄₇Cd₂(TBBT)₃₁ nanoclusters with a Faradaic efficiency of up to 96% for electrocatalytic CO₂ reduction to CO. *Angew. Chem. Int. Ed.* **2020**, *59*, 3073–3077. [[CrossRef](#)]
61. Yuan, X.; Zhang, L.; Li, L.; Dong, H.; Chen, S.; Zhu, W.; Hu, C.; Deng, W.; Zhao, Z.-J.; Gong, J. Ultrathin Pd-Au shells with controllable alloying degree on Pd nanocubes toward carbon dioxide reduction. *J. Am. Chem. Soc.* **2019**, *141*, 4791–4794. [[CrossRef](#)]
62. Sun, K.; Ji, Y.; Liu, Y.; Wang, Z. Synergies between electronic and geometric effects of Mo-doped Au nanoparticles for effective CO₂ electrochemical reduction. *J. Mater. Chem. A* **2020**, *8*, 12291–12295. [[CrossRef](#)]
63. Gao, D.; Zhang, Y.; Zhou, Z.; Cai, F.; Zhao, X.; Huang, W.; Li, Y.; Zhu, J.; Liu, P.; Yang, F. Enhancing CO₂ electroreduction with the metal–Oxide interface. *J. Am. Chem. Soc.* **2017**, *139*, 5652–5655. [[CrossRef](#)] [[PubMed](#)]
64. Kauffman, D.R.; Alfonso, D.R.; Tafen, D.N.; Wang, C.; Zhou, Y.; Yu, Y.; Lekse, J.W.; Deng, X.; Espinoza, V.; Trindell, J. Selective electrocatalytic reduction of CO₂ into CO at small, thiol-capped Au/Cu nanoparticles. *J. Phys. Chem. C* **2018**, *122*, 27991–28000. [[CrossRef](#)]
65. Nie, X.; Esopi, M.R.; Janik, M.J.; Asthagiri, A. Selectivity of CO₂ Reduction on Copper Electrode: The Role of Kinetics of Elementary Steps. *Angew. Chem. Int. Ed.* **2013**, *52*, 2459–2462. [[CrossRef](#)] [[PubMed](#)]
66. Liu, X.; Xiao, J.; Peng, H.; Hong, X.; Chan, K.; Nørskov, J.K. Understanding trends in electrochemical carbon dioxide reduction rates. *Nat. Commun.* **2017**, *8*, 15438. [[CrossRef](#)]
67. Henkelman, G.; Uberuaga, B.P.; Jónsson, H. A Climbing Nudged Elastic Band Method for Finding Saddle Points and Minimum Energy Paths. *J. Chem. Phys.* **2000**, *113*, 9901–9904. [[CrossRef](#)]